International Journal of Rotating Machinery, 8(4): 259–274, 2002

1023-621X/02 $12.00+.00

Nonlinear TURBO Euler Simulation of IGV—Transonic Rotor Interactions

MICHAEL S. RICHMAN and SANFORD FLEETER*
School of Mechanical Engineering, Purdue University, West Lafayette, Indiana 47907, USA

Unsteady aerodynamics is the driving phenomenon for HCF failures of advanced design multistage blade rows. Hence, accurate HCF design analysis is dependent on experimentally validated three-dimensional unsteady aerodynamic blade row interaction CFD codes. Of particular interest herein are the blade row interaction phenomena in transonic compressors. Specifically, the unsteady flow through an IGV row generated by the downstream transonic rotor is simulated with TURBO utilized as an inviscid three-dimensional multistage CFD code. The results of this simulation are then correlated with corresponding benchmark experimental data.

Keywords: Unsteady aerodynamics; Transonic; Forced response; High cycle fatigue

To predict blade life or design blades for longer HCF life, accurate blade unsteady stress predictions are crucial. Current design tools use a finite element description of the blades and an analytical or CFD model of the unsteady aerodynamics of a single blade row. Thus, a number of surprise HCF failures may be a result of the inadequate modeling of strong blade row coupling effects due to the highly unsteady flow.

The driving phenomenon for these HCF failures is the blade row unsteady aerodynamics, specifically blade row interaction and coupling phenomena. Of particular interest are the blade row interaction phenomena in transonic compressors. Specifically, a transonic rotor operates with a supersonic relative velocity with a subsonic axial velocity component, Figure 1. Shocks form near the rotor blade leading edges and propagate upstream into the neighboring upstream vane row. For the closely spaced airfoil rows of advanced design stages, these upstream propagating shocks are a significant forcing function to the upstream vane row, resulting in potential HCF failure.

The prediction of blade row interaction phenomena in transonic compressors is most challenging due to nonlinear aerodynamic and strong blade row coupling effects resulting from the highly unsteady nature of the flow field. For this reason, baseline experimental data must be available to compare with CFD predictions.

Rotor-IGV unsteady aerodynamic interaction phenomena at both transonic and subsonic rotor operating conditions were experimentally investigated by Sanders and Fleeter (1998) and Sanders et al. (1999). Nonlinear interaction effects were significant at the transonic design speed, with very high levels of unsteady loading occurring in the vane trailing edge region due to interactions with the rotor generated shock waves. These nonlinear interactions did not occur at the part-speed operating condition in which the rotor flow was subsonic.

Eulitz et al. (1995) investigated the response of an upstream stator to shocks generated by a downstream rotor using two-dimensional viscous and inviscid analyses. Liamis et al. (1995) analyzed transonic IGV-rotor interactions using a quasi-3D Navier-Stokes analysis. Davis et al. (1996) performed a three-dimensional viscous simulation of the unsteady flow through a transonic compressor, predicting that the unsteady aerodynamic loading on the upstream IGV varies considerably over one cycle due to its interaction with the downstream rotor shock system.

To meet the industry wide need for valid HCF analyses for application to advanced blade rows operating in a multi-blade row environment, time-marching multistage CED analyses are being developed. However, for accurate HCF analyses of advanced blade rows operating in a multi-blade row environment, time-marching multistage CFD analyses must be incorporated into design systems. It is imperative that these analyses be validated with appropriate benchmark multi-blade row flow environment data.

Received 22 September 2000; in final form 9 October 2000.
*Corresponding author. Tel.: 317-494-5622, Fax: 317-494-0539. E-mail: Fleeter@ecn.purdue.edu

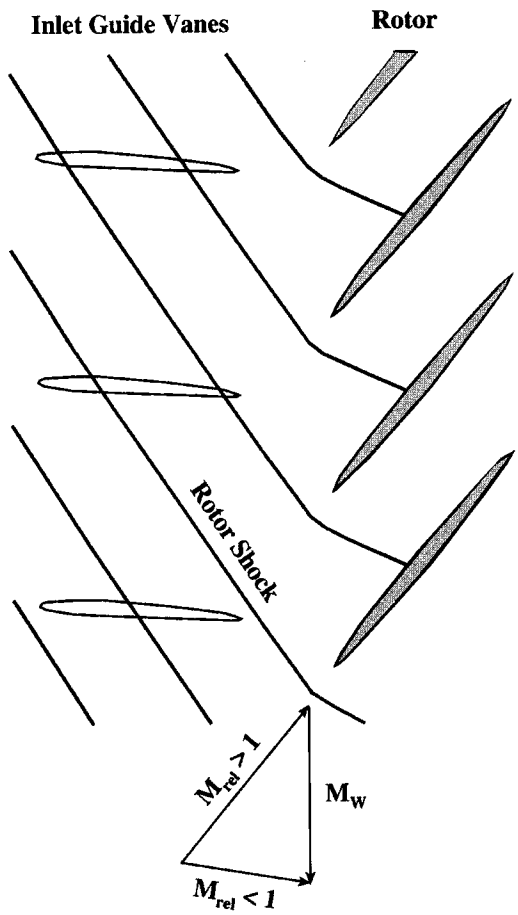

FIGURE 1 Vane excitation due to rotor shocks.

This paper addresses this required validation process for TURBO, an advanced three-dimensional multi-blade row turbomachinery CFD code. A TURBO multi-blade row Euler simulation of this IGV-rotor configuration is implemented and used to simulate the flow through an advanced design transonic compressor IGV row and rotor. The results of this simulation are then correlated with corresponding benchmark data, including both 90% span IGV surface steady and unsteady pressures and the IGV passage flow field.

CFD SIMULATION

TURBO, a NASA-Glenn Research Center developed code, is an Euler/Reynolds-averaged Navier-Stokes three-dimensional unsteady aerodynamic analysis that simulates multistage turbomachinery flow phenomenon, Janus et al. (1992); Chen (1991); Janus and Whitfield (1989). Curvilinear-transformed Navier-Stokes equations are separated into inviscid and diffusive parts, with the terms containing derivatives in the streamwise or ξ direction then neglected.

$$\frac{\partial Q}{\partial \tau} + \frac{\partial F}{\partial \xi} + \frac{\partial G}{\partial \eta} + \frac{\partial H}{\partial \zeta} = \frac{\partial G^d}{\partial \eta} + \frac{\partial H^d}{\partial \zeta} \qquad [1]$$

where Q is the conservative variable matrix, F, G, and H are the ξ, η, and ζ flux vectors, and G^d and H^d are the diffusive dominated flux vectors containing only transformed shear stresses and heat flux terms.

TURBO uses a finite volume scheme discretizing by contiguous volumes of unit lengths, i.e., $\Delta\xi = \Delta\eta = \Delta\zeta = 1$. The formulation is derived by integrating Eq. [1] over a unit volume computational cell. Using the central difference operator $\delta(\delta_l()) = ()_{l+1/2} - ()_{l-1/2})$, the integral form of the thin-layer approximation of the Navier-Stokes equations is obtained.

$$\frac{\partial Q}{\partial \tau} = -\delta_i(F) - \delta_j(G - G^d) - \delta_k(H - H^d) \qquad [2]$$

The connective flux vectors F, G, and H are hyperbolic type flux vectors and homogenous functions of the first degree, enabling the use of an implicit upwind difference method. The diffusive dominated flux terms G^d and H^d are treated explicitly. The flux Jacobians are evaluated by flux vector splitting and Roe's flux difference splitting to form a higher-order total-variation-diminishing (TVD, non-oscillatory) scheme to evaluate the residual fluxes.

Newton sub-iterations are used for each time step to provide a converged (steady) solution within the unsteady time step, with symmetric Gauss-Seidel iterations, Eq. [3], applied to the discretized equations.

$$x_i^{(k+1)} = \frac{1}{a_{ii}}\left(b_i - \sum_{j=1}^{i-1} a_{ij}x_i^{(k+1)} - \sum_{j=i+1}^{n} a_{ij}x_j^{(k)}\right) \qquad [3]$$

where $i = 1, \ldots, n$ and $Ax = b$ form the set of discretized equations.

TRANSONIC RESEARCH COMPRESSOR

The Purdue Transonic Multistage Research Compressor features a $1\frac{1}{2}$-stage axial-flow geometry representative of that used in the front stages of advanced aircraft engine high-pressure compressor designs. The test section has a constant hub-tip ratio of 0.67 with a tip diameter of 0.3 m (12.0 in.) and features an inlet guide vane (IGV) row, a blisk with 19 rotor blades, and a downstream stator row, Figure 2. The rotor blades consist of NACA 65 series

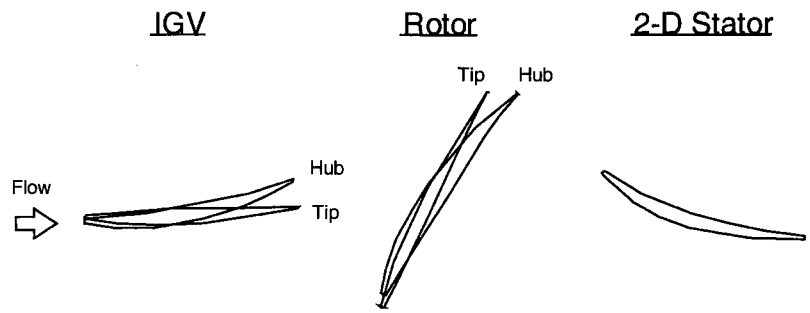

FIGURE 2 Compressor geometry.

profiles on circular arc meanlines with a 5.08-cm (2.0-in.) chord and a thickness distribution varying from 10% at the root to 6% at the tip. The IGV and stators are an advanced controlled diffusion airfoil (CDA) design with a 4.45-cm (1.75-in.) chord and a constant 7% thickness. The IGV-rotor and rotor-stator mid-span axial spacings are 41.4% and 39.0% vane chord, with the IGV and stator rows each having 18 vanes set at their design stagger angles.

The unsteady flow field in the upstream IGV passage generated by the downstream rotor has been experimentally investigated. Detailed IGV surface steady and unsteady pressure data and IGV passage flow field data

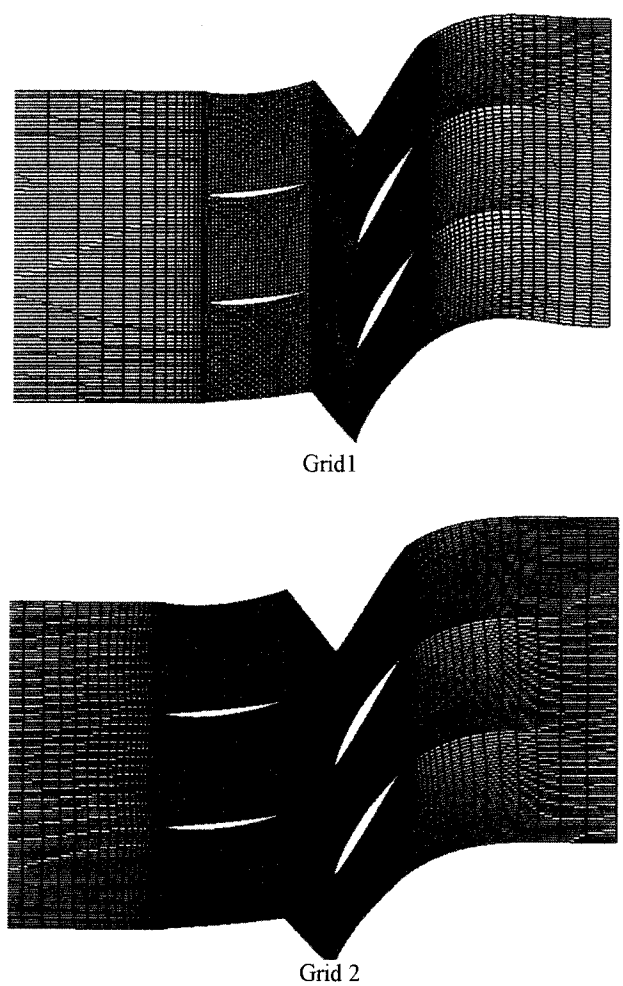

FIGURE 3 Computational grid shown for 3 passages.

were acquired at 100% ($N_c = 20{,}000$ rpm) design speed, resulting in transonic flow through the rotor. At 90% span, the potential flow generated forcing function to the IGV's generated by the rotor was measured with an unsteady static pressure probe, with the resultant 90% span IGV surface unsteady aerodynamic response determined by high-response dynamic pressure transducers, Sanders and Fleeter (1998). Particle Image Velocimetry (PIV) measurements quantified the steady and unsteady flow through the IGV passages, Sanders et al. (1999).

COMPUTATIONAL GRID

The three-dimensional multi-block grids for the simulation are generated with TIGER (Turbomachinery Interactive Grid GenERator). Figure 3 shows an airfoil-to-airfoil view of the computational grids at 50% span. The three-dimensional grid is divided into two blocks, one for the IGV and one for the rotor. Grid 1 contains 30 vane passage points, 20 uniformly distributed spanwise points, and 53 axial points with 30 points on the vane surface. Similarly, the rotor grid 1 block contains 30 blade passage points, 20 uniformly distributed spanwise points, and 68 axial points again with 30 points on the blade. The split between the IGV and rotor grid block was chosen to be the center of the stage spacing. To more accurately capture the unsteady IGV/rotor interaction, Grid 2 was generated increasing the grid density from 72,600 nodes to 320,000. To reduce computational expense, the stator was not modeled for both grids. Pressure ratios were adjusted accordingly for each operating point.

RESULTS—IGV AND ROTOR FLOW FIELDS

The simulation of the transonic rotor-IGV interaction is performed on a Silicon Graphics-Octane with a single 250 Mhz RS-10000 processor, 1 Gig RAM, and a 13 Gig hardrive. To speed up processing time and reduce memory requirements, the simulation was reduced to include only the IGV and rotor rows, thereby saving approximately 80 meg of ram and reducing the required CPU time by one third for grid 1 with similar proportional savings with grid 2. Also, the TURBO simulations are based on an 18 IGV-18 rotor blade configuration, thereby reducing the actual rotor solidity by 5% and changing the IGV-rotor interblade phase angle from $-20°$ to $0°$.

Compressor Performance

Input for initializing the TURBO simulation consists of the pressure ratio (static-to-static), the freestream Mach number, and the rotor speed. The predicted and measured compressor performance maps are shown in Figure 4.

The TURBO predictions closely match the data at both the rotor transonic design speed (20,000 rpm) and part-speed (15,000 rpm) operating points. The Euler simulation

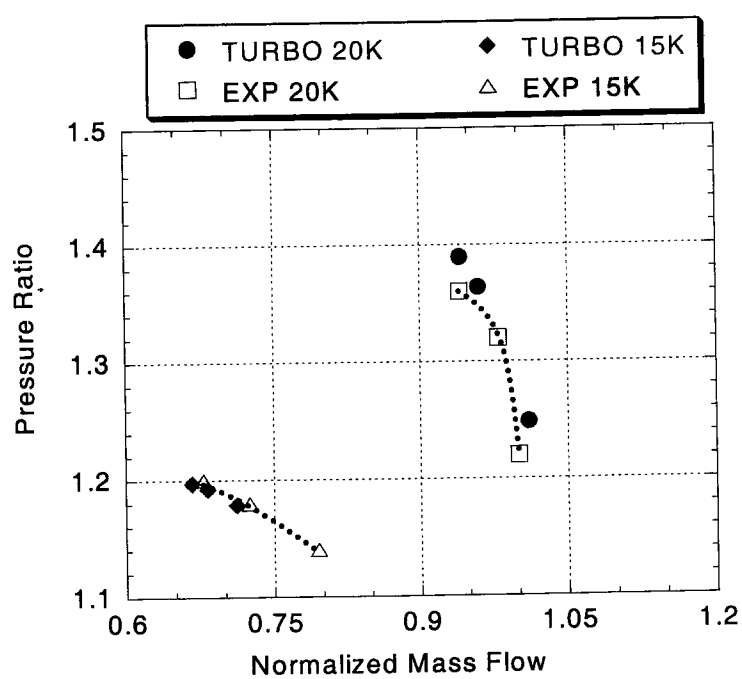

FIGURE 4 Measured and simulated compressor map.

yielded a pressure ratio an average of 2.6% higher than measured at design speed and 1.5% higher at part-speed and also a 1.2% higher mass flow at the maximum flow condition (free-stream Mach number = 0.35, pressure ratio = 1.0, rotor speed = 20,000 rpm). The scaling of the geometry from the 18 IGV's and 19 rotor blades of the compressor to the 18 IGV's and rotor blades of the simulation affects these results, changing the mass flow on a specific speed line as well as creating the 1.2% delta at max flow conditions. However, the simulations are at the same relative operating points on the compressor map.

IGV and Rotor Flow Fields

The effect of rotor speed on the IGV and rotor passage flow field at 10%, 50% and 90% span is shown in Figures 5 and 6. Presented are the normalized instantaneous static pressure contours at the part-speed 15,000 rpm and design 20,000-rpm conditions.

The flow is subsonic at all three spanwise locations for the 15,000 rpm operating point. The flow characteristic is essentially the same throughout the span. However the rotor potential field impingement on the trailing edge of the IGV is most evident at the 90% span location, diminishing in strength toward the hub. This rotor-IGV interaction causes uneven loading in the trailing edge region of the IGV's, indicating that the IGV-rotor interactions are important at this part-speed condition, as shown by the 180° phase difference between suction and pressure side surface pressures. TURBO predicts a maximum peak-to-peak unsteady surface pressure of 20% of the inlet total pressure.

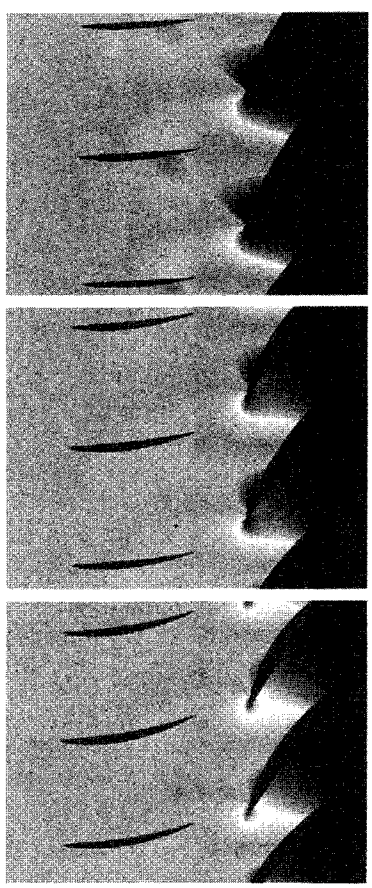

FIGURE 5 Part-speed predicted IGV and rotor instantaneous flow fields.

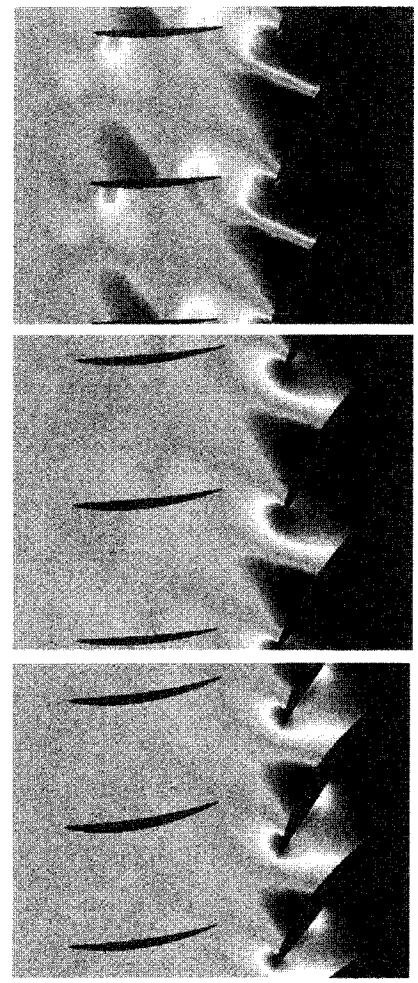

FIGURE 6 Design-speed predicted IGV and rotor instantaneous flow fields.

Figure 6 shows that a detached bow shock forms on the rotor at the design speed that is strongest at 90% span and continues to the hub although it diminishes in strength. This shock extends from approximately 70% chord on the adjacent rotor blade to the trailing edge of the IGV where it splits, reflects, and continues upstream into the IGV passage.

Figures 7 and 8 present the rotor blade surface Mach distribution for both part-speed and design-speed operating

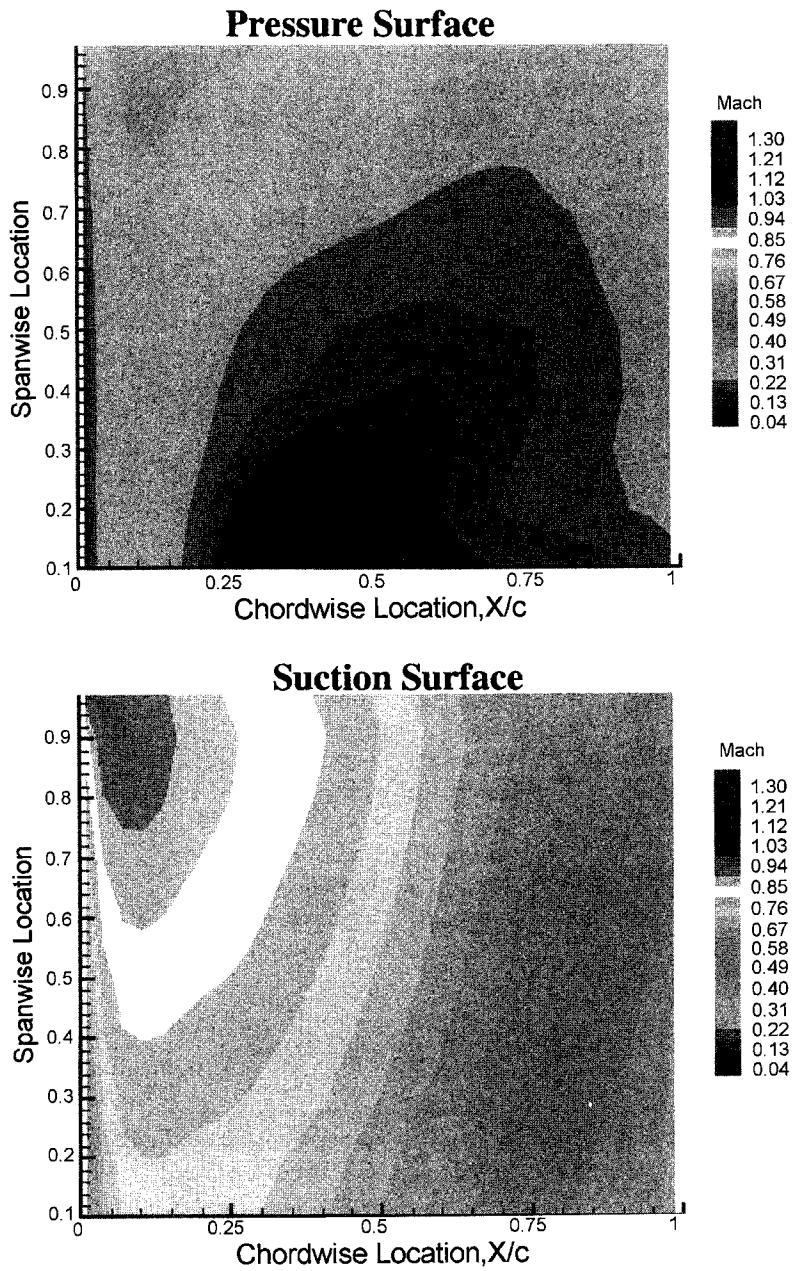

FIGURE 7 Predicted rotor blade surface Mach distribution (15,000 rpm).

conditions. At part-speed, the flow is subsonic over both rotor blade surfaces. At the design-speed of 20,000 rpm, however, a shock spans the entire rotor blade suction surface, with a maximum Mach number of approximately 1.3.

IGV SIMULATION—DATA CORRELATION

The predictions of the IGV steady flow and the rotor-IGV interaction generated unsteady aerodynamics on the IGV row at 90% span for both subsonic and transonic rotor conditions are correlated with corresponding benchmark data, including both surface steady and unsteady pressures and the IGV passage flow field.

Part-Speed 15,000 RPM

Figures 9 and 10 show the data-simulation correlation of the IGV time-average flow field and surface pressures. Grid 1 and Grid 2 both result in relatively accurate predictions of the time-average characteristics, providing

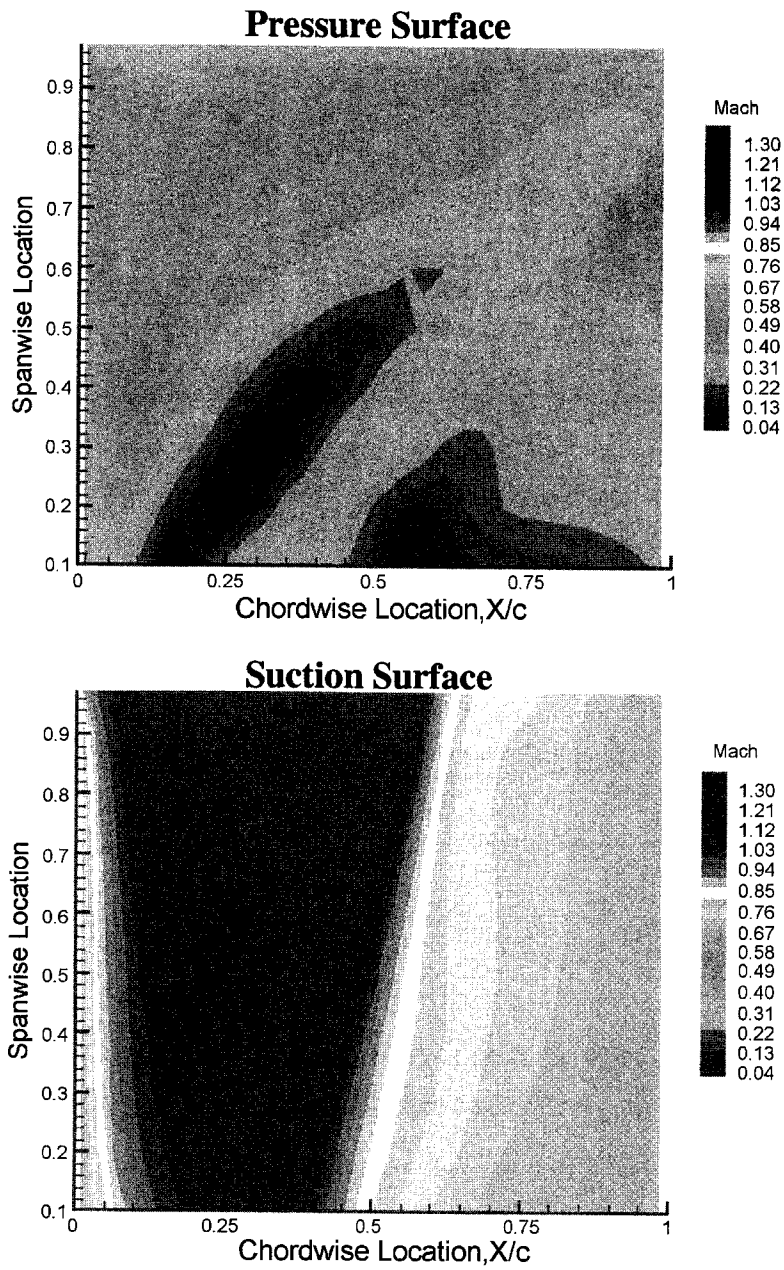

FIGURE 8 Predicted rotor blade surface Mach distribution (20,000 rpm).

results within 2% of measured surface pressure data. Figure 9 provides a qualitative comparison, showing that in general TURBO properly predicts the time-average IGV passage flow structures using both grid densities. However, even with the higher fidelity grid, TURBO does not predict the high Mach number structure on the pressure surface starting at approximately midchord. TURBO calculates this structure beginning farther upstream on the IGV surface. This can be seen in Figure 10 where TURBO underpredicts the pressure surface pressures near the leading edge.

Blade row interactions are significant even at part-speed, as was clearly evident in the IGV–rotor flow field predictions previously presented in Figure 5. The simulation of this unsteady aerodynamic interaction is critical to the accurate prediction of the IGV row unsteady aerodynamics and HCF, specifically the rotor generated forcing function to the IGV row and the resultant IGV unsteady aerodynamics which drive the IGV response. Figure 11 shows that the TURBO predicted rotor generated unsteady aerodynamic forcing function to the IGV's closely matches that measured experimentally. However, the predicted

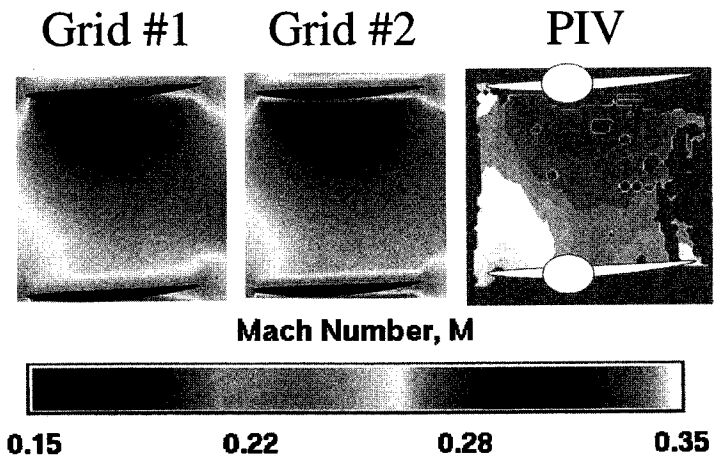

FIGURE 9 Time average IGV Flow Field Correlation Part Speed (15,000 rpm).

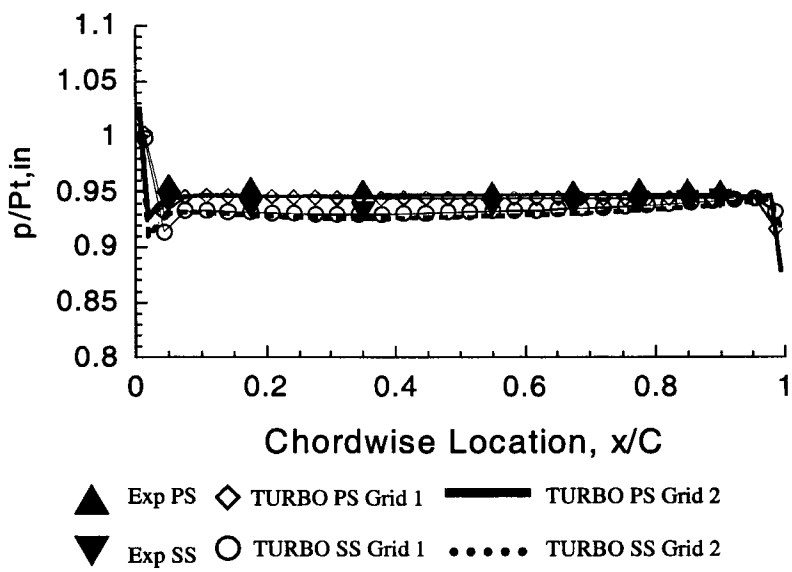

FIGURE 10 Time Average IGV Surface Pressure Correlation Part-Speed (15,000 rpm).

forcing function waveforms do not contain the measured higher harmonics of blade pass frequency, particularly the Grid 1 results. This result is also evident in Figure 12 which shows the power spectrum of the forcing function data and simulation results. Grid refinement is seen to provide a more accurate prediction, with TURBO simulating up to the 4th harmonic of blade pass frequency with Grid 2.

Figure 13 compares the 90% span predicted and measured IGV passage flow field for one rotor blade pass period at the part speed condition. There is good agreement between the predicted and measured IGV passage flow structures, analogous to the time-average correlation results. Grid refinement between Grids 1 and 2 is most evident for part-speed operation. Clearly, doubling the number of grid points along the IGV surface and within the vane passage provides a more accurate prediction, avoiding the "smearing" of the flow field structures. The rotor generated potential field traverses upstream through the IGV passage, pushing a higher Mach structure along the pressure surface. This characteristic virtually disappears at $t/T_{bp}=4$ when simulated with Grid 1, whereas Grid 2 maintains both the structure magnitude and relative location with the PIV data. The effect of the simulation geometry scaling can also be seen throughout the rotor blade pass period, with the rotor potential field predicted farther upstream for a given rotor position.

Figure 14 shows the IGV time-variant surface pressures over one rotor blade pass period. The overall prediction and data exhibit trendwise agreement, with TURBO generally under-predicting the magnitude of the unsteady

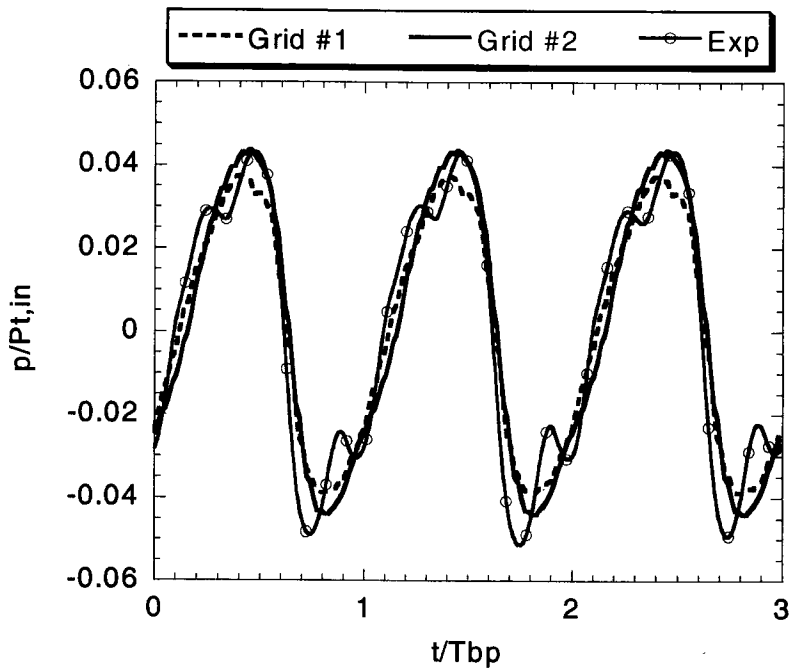

FIGURE 11 Part-Speed IGV forcing function correlation.

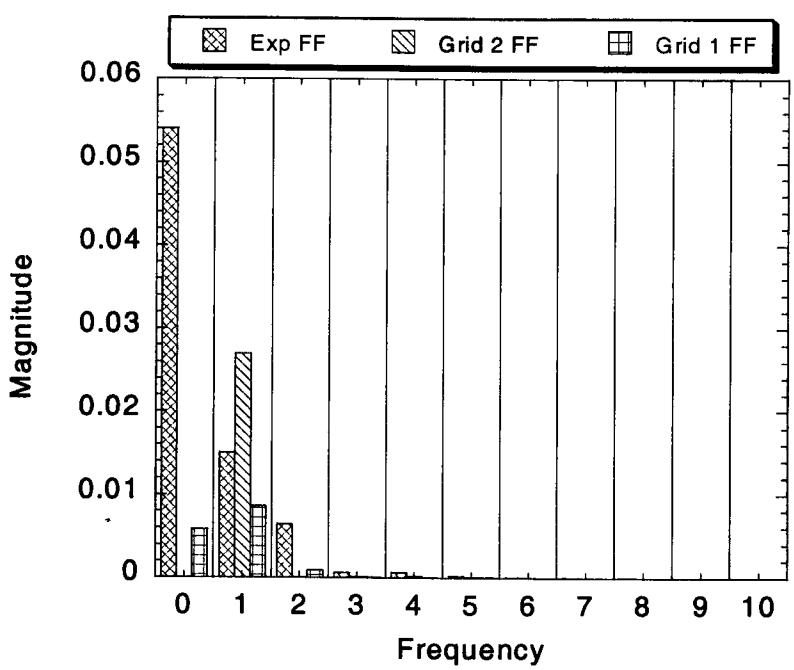

FIGURE 12 Part-speed forcing function harmonic content (power spectrum).

pressure data for Grid 1. These results clearly show that higher grid densities are required to properly capture the quantitative effects of the rotor generated potential field.

Unsteady flow characterization is the key to properly predict HCF blade failures. Figure 15 shows that the simulation using Grid 1 is not able to predict the IGV surface unsteady pressure waveforms, only capturing the pressure magnitude on the pressure surface at 90% chord and at the 17.5% chord on the suction surface. Following the trend established with the IGV surface unsteady pressure correlation, Grid 2 improves the IGV surface pressure waveform predictions, matching the magnitude well at the

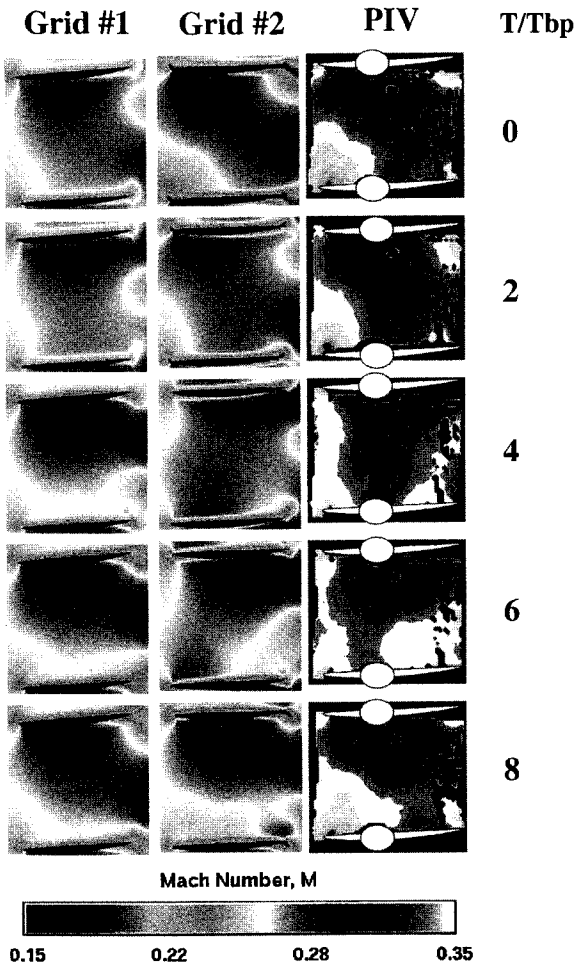

FIGURE 13 Part speed IGV unsteady flow field correlation, 90% Span.

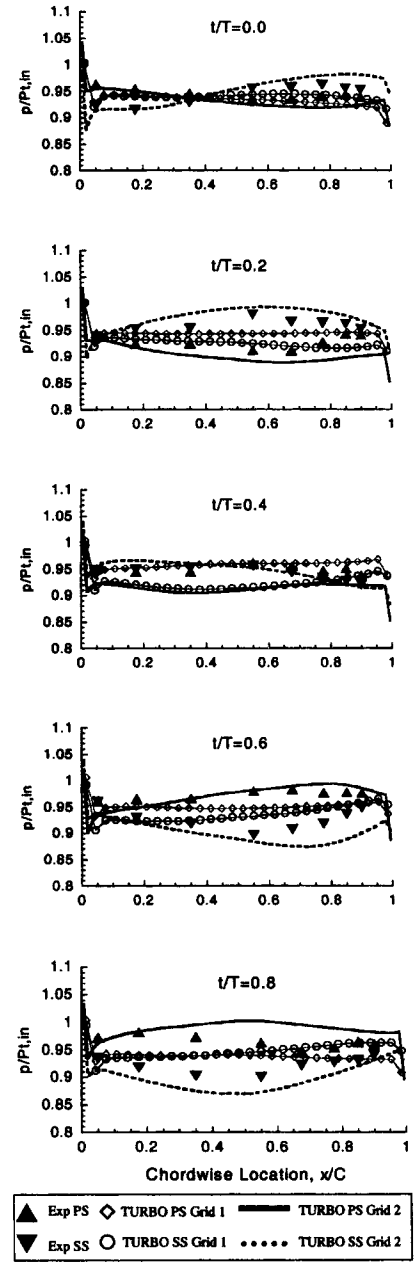

FIGURE 14 Part-speed IGV unsteady surface pressure correlation, 90% span.

leading edge, yet progressively overpredicting toward the trailing edge.

TURBO has been shown to accurately predict the IGV row steady flow characteristics. However, the TURBO unsteady flow simulations show only trendwise agreement with the data, with Grid 1 generally underpredicting the surface pressure magnitudes and Grid 2 overpredicting them, albeit closer. Qualitatively, TURBO accurately predicts the flow structures and surface pressure characteristics. The time-average and unsteady lift data-simulation correlation results, Figures 16 and 17, show that the time-average lift is underpredicted by 23.8% with Grid 1 and overpredicted by 16% with Grid 2, with the Grid 1 unsteady lift out-of-phase for 60% of the blade pass period. At times during the blade pass period, the unsteady lift predicted with Grid 1 differs from the corresponding data by as much as 370%. Grid 2 improves on the phase, reducing the out-of-phase prediction from 60% to 20% of the rotor pass period. However, the unsteady lift magnitude is overpredicted by a maximum of 62% at $t/T_{bp} = 0.7$. Thus, even though Grid 2 improved both the flow field and surface pressure predictions, the unsteady lift correlation illustrates the difficulty in simulating this highly unsteady flow.

Design Speed—20,000 RPM

Figures 18 and 19 present the TURBO time-average flow field and surface pressure predictions at 90% span and

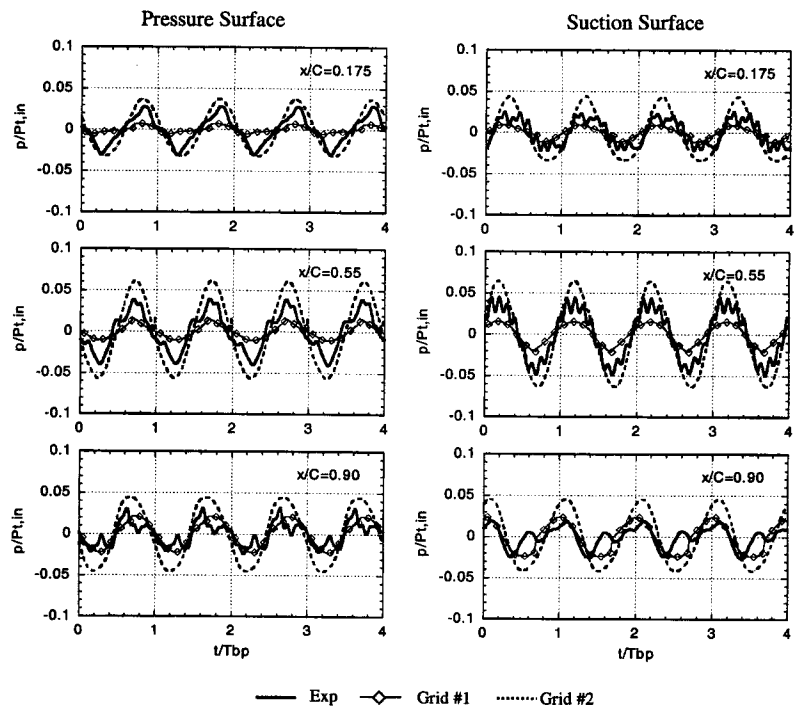

FIGURE 15 Part-speed IGV surface pressure unsteady waveform correlation.

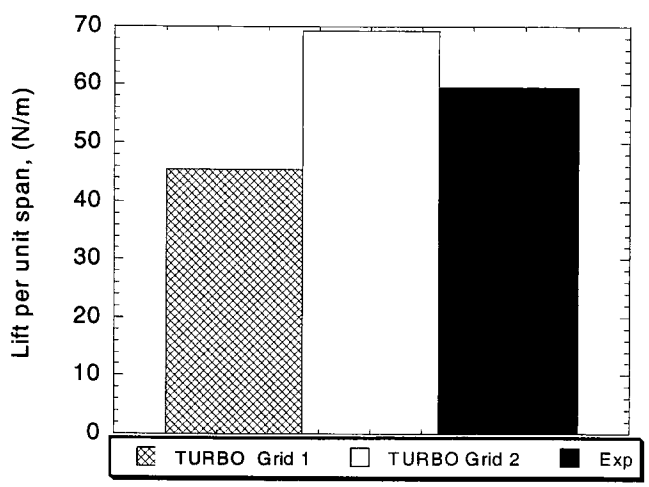

FIGURE 16 Part-speed time average IGV lift correlation, 90% span.

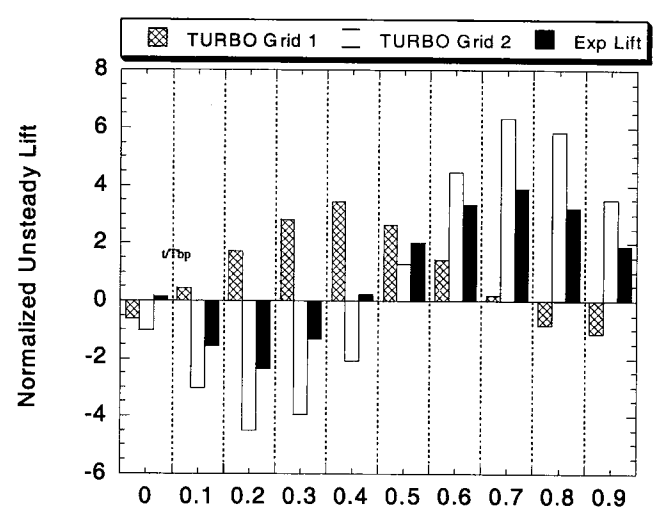

FIGURE 17 Part-speed unsteady IGV lift correlation, 90% span.

20,000 rpm (design speed). Analogous to the part-speed results, the correlation of the time-average IGV flow field TURBO simulation with the data is relatively good. Also, at this operating condition, there is little difference between the predictions with Grids 1 and 2. The IGV surface time-averaged pressure data trend is well predicted by TURBO, with a maximum difference between the prediction and data of 1.7% with Grid 2 at 17% chord. Again, both grids show good trendwise correlation with the data.

TURBO predicts the fundamental characteristics of the rotor generated forcing function very well, Figure 20, but does not predict the higher order modes apparent in the data, Figure 21. The Grid 1 simulation overpredicts the measured forcing function minimum by 80% and predicts the maximum by 18%. The increased grid density avoided possible "smoothing" of the unsteady forcing function characteristic and improved the overall prediction of this interstage dynamic pressure measurement. Despite the improvement, Grid 2 underpredicts the peak by 18% and

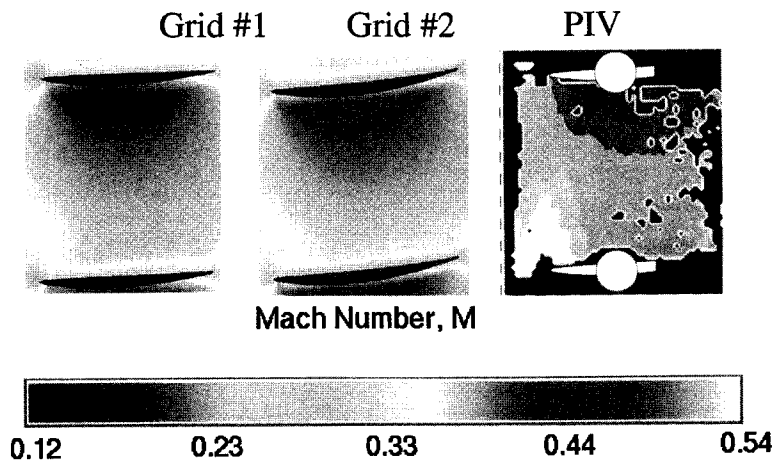

FIGURE 18 IGV passage time-averaged flow fields.

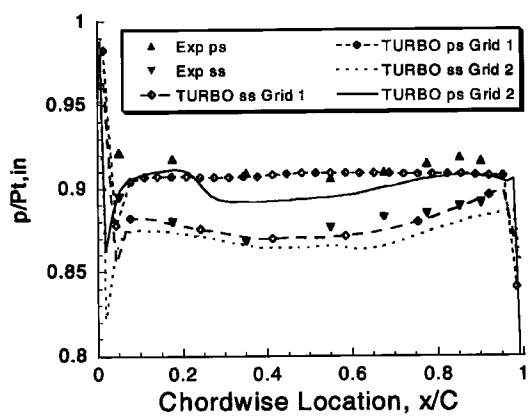

FIGURE 19 Time-average IGV surface pressure correlations at 90% span, 20,000 rpm.

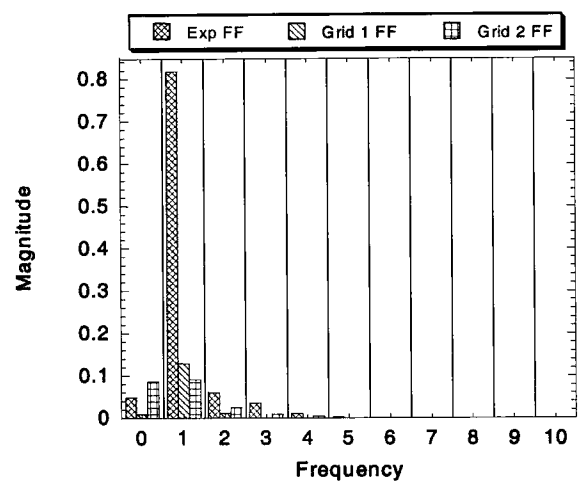

FIGURE 21 Design-speed forcing function harmonic content (power spectrum).

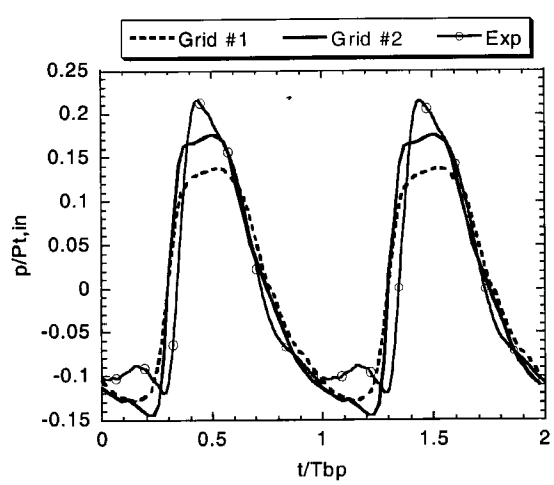

FIGURE 20 Design-speed IGV forcing function correlation.

overpredicts the minimum by 20%, i.e., the prediction is essentially an offset curve from the data.

The improvement in the forcing function data-simulation correlation due to the grid refinement carries over to the power spectrum (PS) correlation. Higher harmonics in the measured signal are also present in the Grid 2 prediction, although with lower magnitudes.

The 90% span simulation and the measured unsteady IGV passage flow field, i.e., the IGV passage Mach contours, for one rotor blade pass period are shown in Figure 22. The progression of the time-variant IGV flow field starts at the top with the initial impingement of the rotor leading edge shock on the IGV trailing edge.

The simulation and the IGV passage flow field data exhibit good qualitative correlation, specifically the rotor shock interactions with the IGV's. However, the Grid 1 prediction smoothes out certain details, for example the

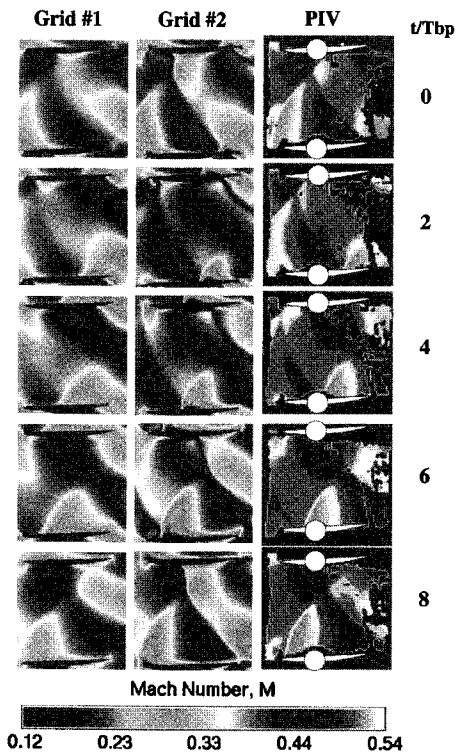

FIGURE 22 Design-speed IGV passage flow field correlation.

reflection of the shock as it strikes the IGV pressure surface. This is most evident at the beginning of the rotor blade pass period where the PIV data show the interaction of the shock with the reflected shock from the previous rotor blade. TURBO with Grid 1 predicts a much milder reflected shock and, thus, a diminished interaction. Grid 2 dramatically improves this prediction, providing a sharp shock and showing distinct interaction with adjacent rotor blade shocks as measured with PIV. This improvement continues throughout the rotor blade pass period, accurately predicting the magnitude and flow structure.

The result of scaling the rotor geometry from 19 to 18 blades is most evident in this IGV flow passage data-prediction correlation. Namely, as the rotor shock first impacts the IGV trailing edge, the PIV data show that the interaction with the reflected shock from the previous rotor blade occurs at midchord. However, the simulation predicts that this interaction occurs further upstream, at approximately 30% chord. Interestingly, Grid 2 does improve in this area, yet the inter-blade phase angle scaling effect remains.

The predicted and measured IGV time-variant surface pressures over one rotor blade pass period are shown in Figure 23. The data and prediction exhibit similar trends, showing the upstream travelling pressure wave generated by the passing of the downstream rotor. The simulation correctly predicts the 180° phase difference between the response of the IGV pressure and suction surfaces,

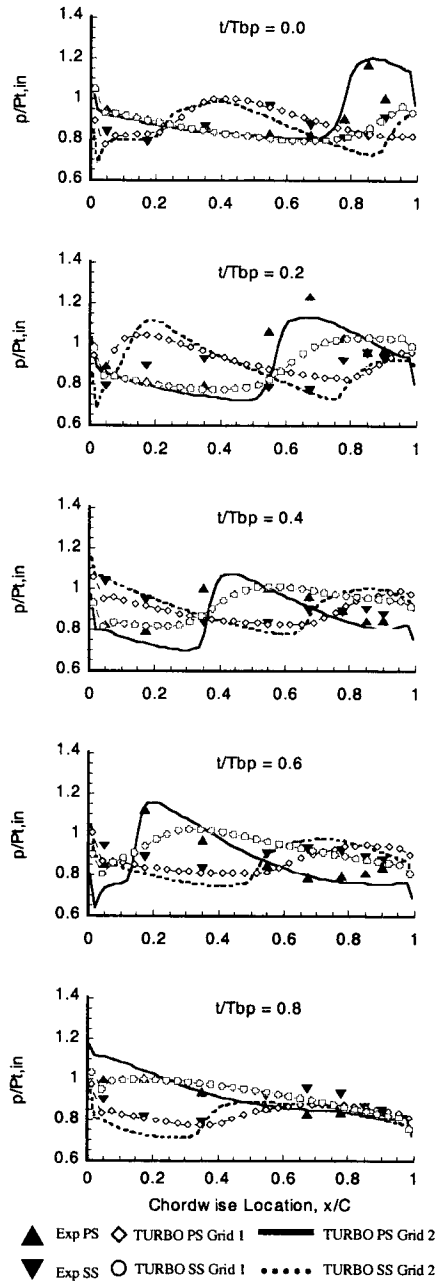

FIGURE 23 Design-speed 90% span IGV surface pressure correlations.

although Grid 1 has difficulty in the trailing edge region. Specifically, the pressure peak of the shock impinging on the IGV trailing edge is smoothed over in the simulation. This was the primary motivation for investigating grid effects on the TURBO simulation. The unsteady surface pressures must be accurately modeled to properly predict the unsteady aerodynamic forces driving blade/vane vibrations and HCF. Additional grid points in the inter-stage region and along the vane surface allow TURBO to capture the unsteady pressure peaks as the shock wave travels forward along the IGV.

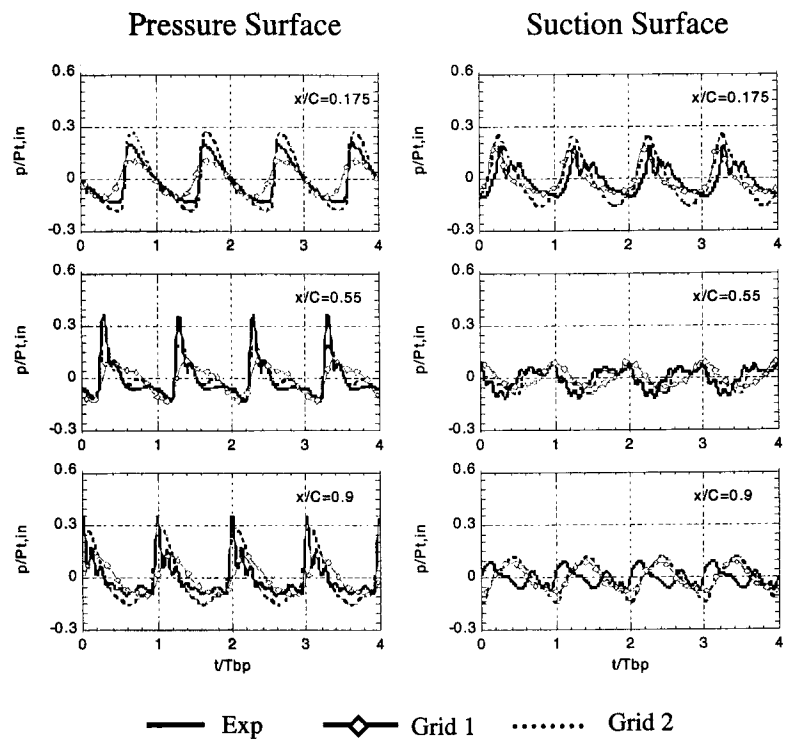

FIGURE 24 Design-speed 90% span IGV pressure waveform correlation.

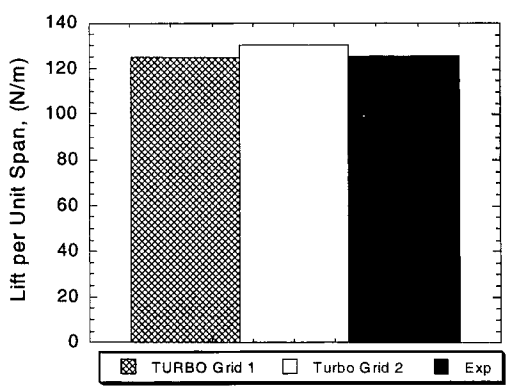

FIGURE 25 Design-speed 90% span IGV time average lift correlation.

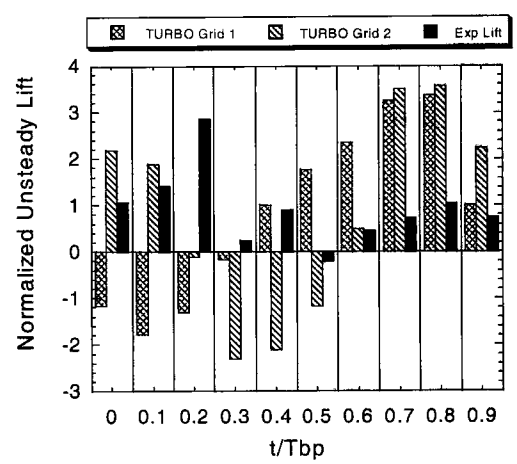

FIGURE 26 Design-speed 90% span IGV unsteady lift correlations.

The correlation of the predicted and measured IGV surface pressure waveforms, Figure 24, shows analogous results. The Grid 1 simulation generally does not predict the measured surface unsteady pressure waveforms, and thus provides insight into difficulties with the trailing edge steady and unsteady predictions previously noted. Specifically, the measured pressure surface waveform fluctuations are very sharp and impulse-like over the IGV aft 30% chord. However, TURBO predicts a smooth waveform. In fact, with Grid 1, TURBO increasingly underpredicts the unsteady surface pressure from the IGV leading to trailing edge where as with Grid 2, the predictions follow the magnitude data.

TURBO has been shown to accurately predict the measured IGV time-average flow characteristics. This is reflected in the correlation of the predicted and measured time-average lift, Figure 25. There is less than 1.0% difference between the prediction and the data for both grids.

The correlation of the predicted and measured unsteady lift, however, is poor, Figure 26. The Grid 1 TURBO simulation is out-of-phase with the data for 50% of the rotor blade pass period and the unsteady lift prediction

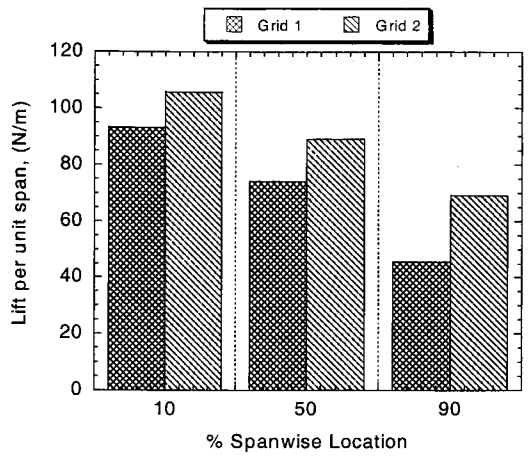

FIGURE 27 Part-speed IGV spanwise time-average lift.

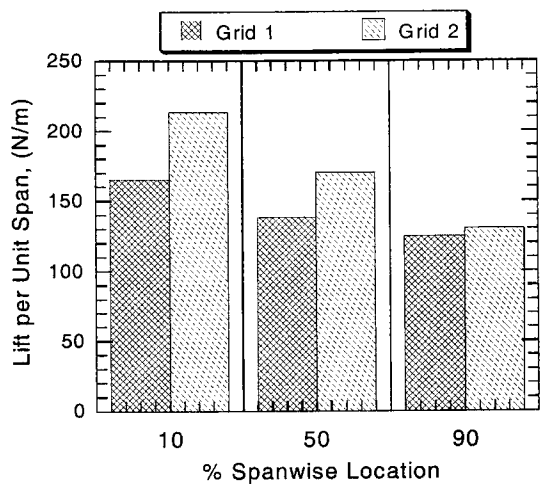

FIGURE 28 Design-speed IGV spanwise time-average lift.

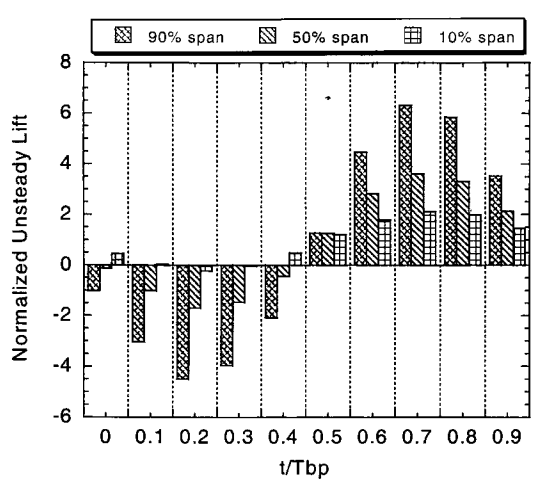

FIGURE 29 Part-speed IGV unsteady spanwise lift Grid 2.

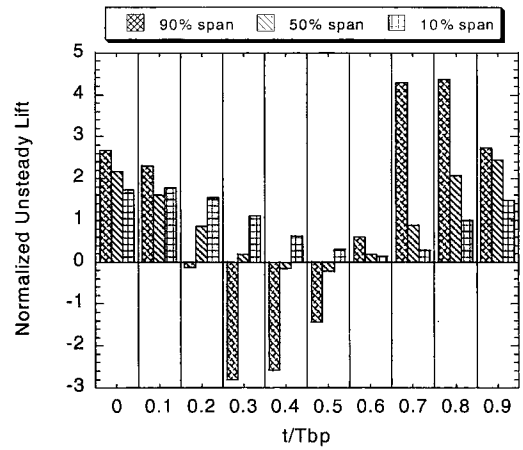

FIGURE 30 Design-speed IGV spanwise unsteady lift Grid 2.

differs from the data by as much as 338%. Even though Grid 2 dramatically improved the time-average and unsteady flow field and surface pressure correlations with the data, TURBO still predicts a normalized unsteady lift which is 180° out-of-phase for 30% of the rotor blade pass period, with a maximum difference of 374% at $t/T_{bp} = 0.7$.

3-D IGV Flow Field Predictions

The predicted IGV time-average loading at hub, mid-span, and tip is shown in Figures 27 and 28. The time-average loading increases from tip-to-hub, by 32.4% at 20,000 RPM and 64% at 15,000 RPM, corresponding to the increase in the IGV camber. For both operating conditions, Grid 2 results in higher lift per unit span, as per the previous results where increasing grid density seemed to improve the flow prediction.

Figures 29 and 30 demonstrate the three-dimensionality of the unsteady flow field at part-speed and design speed conditions. The simulation shows that the 90% span unsteady lift is opposite in magnitude (relative to 50% and 10% span locations) over 30% of one rotor blade pass period at design speed, resulting in a maximum IGV unsteady lift difference (hub-to-tip) for one rotor blade pass period of 256% at part-speed and 451% at design rotor speed. While the design speed 90% span time-variant loading varies in and out of phase with respect to the mid-span and hub, the mid-span and hub time-variant loading forces the blade in the same direction at both part-speed and design-speed for 80% of the rotor pass period.

The span loading envelope (10% − 90% span) ranges from 390% time-average lift at $t/T_{bp} = 0.3$ to 93% time average lift at $t/T_{bp} = 0.0$, showing the strength of the design speed rotor shock interaction as compared to the part-speed potential field interaction where loading envelopes range from 394% time-average lift at $t/T_{bp} = 3$ to 6% time-average

lift at $t/T_{bp} = 5$. Clearly, the potential field generated at part-speed operation can provide significant pressure fluctuations along the IGV surface.

CONCLUSIONS

Unsteady aerodynamics is the driving phenomenon for HCF failures of advanced design multistage blade rows. Hence, accurate HCF design analysis is dependent on experimentally validated three-dimensional unsteady aerodynamic blade row interaction CFD codes. Of particular interest herein are the blade row interaction phenomena in transonic compressors. This paper has addressed this required validation process for TURBO, an advanced three-dimensional multi-blade row turbomachinery CED code. This was accomplished by implementing a TURBO multi-blade row Euler analysis and applying it to simulate the flow through an advanced design transonic compressor IGV row and rotor. This simulation was then correlated with corresponding benchmark data.

The simulation demonstrated the three dimensionality of the IGV passage flow field. The rotor design-speed bow shock and the part-speed potential field forcing function to the upstream IGV row diminished from a maximum near the IGV tip to a minimum near the hub.

The TURBO predictions very closely matched the measured compressor performance map at the rotor transonic and part speed operating conditions. Also, the correlation of the predicted and measured IGV passage flow field showed that the simulation geometry scaling for computational efficiency resulted in predicting the rotor shock and potential field farther upstream throughout the rotor blade pass period.

The rotor-IGV interaction simulation exhibited qualitatively good correlation with the IGV passage flow field data. However, there were important quantitative differences. TURBO overpredicted the magnitude of the IGV steady surface pressures while underpredicting the magnitude of the unsteady component, primarily in the trailing edge region for Grid 1. Via grid refinement, this was attributed to an inadequate number of grid points in the interstage region as well as along the vane surface.

The overarching goal of CFD with regard to HCF design analysis is to accurately predict the unsteady forcing function and the resulting airfoil row unsteady aerodynamics. TURBO predicted the fundamental characteristic of the rotor generated forcing function, but not the higher order modes apparent in the data. Also, TURBO did not accurately predict the phase or magnitude of the unsteady lift on the IGVs even though the refined grid accurately captured the IGV flow field and unsteady surface pressures.

Acknowledgments

The Air Force Office of Scientific Research (AFOSR), the NASA Glenn Research Center, and the Propulsion and Power Research and Engineering Department of Naval Air Systems Command (NAVAIR) sponsored this research. This support is most gratefully acknowledged.

NOMENCLATURE

F, G, H	curvilinear coordinate flux vectors
G^d, F^d	diffusive portion of flux vectors
Q	curvilinear coordinate conservative variable vector
ξ, η, ζ	curvilinear coordinates
τ	time in computational space
δ	central difference operator

REFERENCES

Sanders, A. J. and Fleeter, S. (1998) "An Experimental Investigation of IGV-Rotor Interactions in a Transonic Axial-flow Compressor", *AIAA Paper*, 98–3291.

Sanders, A. J., Papalia, J. and Fleeter, S. (1999) "A PIV Investigation of Rotor-IGV Interactions in a Transonic Axial-flow Compressor", *AIAA Paper*, 99–2674.

Eulitz, F., Engel, K. and Pokorny, S. (1995) "Numerical Investigation of Inviscid and Viscous Interaction in a Transonic Compressor", *Propulsion and Energetics Panel 85th Symposium*, Derby, United Kingdom, May 8–12, AGARD-CP-571.

Liamis, N., Bacha, J. L. and Burguad, F. (1995) "Numerical Simulations of Stator-Rotor Interactions on Compressor Blade Rows", *Propulsion and Energetics Panel 85th Symposium*, Derby, United Kingdom, May 8–12, AGARD-CP-571.

Davis, R. L., Shang, T., Buteau, J. and Ni, R. H. (1996) "Prediction of 3-D Unsteady Flow in Multi-Stage Turbomachinery Using an Implicit Dual Time-step Approach", *AIAA Paper*, 96–2565.

Janus, M. J., Horstman, H. Z. and Whitfield, D. L. (1992) "Unsteady Flowfield Simulation of Ducted Prop-fan Configurations", *AIAA Paper*, 92–0521.

Chen, J. P. (1991) "Unsteady Three-dimensional Thin-layer Navier–Stokes Solutions for Turbomachinery in Transonic Flow". *Ph. D. Dissertation*, Mississippi State University.

Janus, M. J. and Whitfield, D. L. (1989) "A Simple Time-accurate Turbomachinery Algorithm with Numerical Solutions of an Uneven Blade Count Configuration", *AIAA Paper*, 89–0206.